RESEARCH ARTICLE

NANO · MICRO small
www.small-journal.com

Dual Catalytic Mechanism of Co-Doped Amorphous Nickel Phosphate Catalysts in Nucleophilic Oxidation Reactions

Jianhua Shen, Can Hong, Yanbin Qi, Yihua Zhu, Hongliang Jiang, and Chunzhong Li**

Facing the fossil energy crisis and environmental issues, developing renewable energy is urgent, with green hydrogen being crucial in energy transition but electrolytic water hydrogen production has high costs needing solutions, such as replacing oxygen evolution reaction (OER) with organic oxidation reactions. Here, Co-doped amorphous nickel phosphate materials (Co-NiP$_x$O$_y$/NF) are synthesized via electrodeposition and applied as catalysts for the methanol oxidation reaction (MOR). The 10% Co-doped material demonstrates remarkable efficacy in catalyzing MOR. When compared to the OER, it reduced the applied potential required to reach a current density of 200 mA cm^{-2} by 227 mV. During constant-current electrolysis at current densities ranging from 20 to 250 mA cm^{-2}, the Faraday efficiencies (FE) of the formate products consistently exceeded 90%, and the catalysts maintained stable electrolysis for 120 h. into and discussed the action mechanism of Co-NiP$_x$O$_y$/NF is delved, proposing a dual-mechanism model involving hydrogen vacancy oxygen and electrophilic OH* species. These findings provide a solid theoretical foundation for the rational design and modification of catalysts, thereby paving the way for the development of a more efficient and cost-effective electrolytic water–based hydrogen production technology.

1. Introduction

Fossil energy is crucial for human survival. But the severe energy shortage and environmental problems from burning fossil fuels make developing and using renewable and clean energy urgent.[1,2] Green hydrogen from renewable sources is an important energy carrier for the future.[3,4] Electrolysis of water driven by renewable energy will be the main way to prepare green hydrogen, but it's costly now.[5,6] The high cost is due to the high energy consumption of the anode oxygen evolution reaction (OER).[7] The anodic reaction OER involves four electron transfers, is slow, needs high overpotentials, and the product, oxygen, has low economic value.[8–10] Replacing OER with the oxidation of organic matter and coupling it with the hydrogen evolution reaction (HER) semi-reaction can reduce the electricity cost of electrolysis.[11] It can be implemented at the anode as an effective strategy for producing high-value-added products or degrading wastewater.[12–14]

Organic oxidation reactions are called nucleophilic oxidation reactions (NOR).[15] Nickel-based catalysts often exhibit relatively high catalytic activity for organic oxidation reactions in alkaline media. They are commonly used in the electrocatalytic oxidation of organic compounds such as monohydric alcohols,[16,17] polyols,[18,19] aldehydes,[20,21] amines,[22,23] and amides.[24] However, its catalytic mechanism remains controversial. The catalytic mechanism is crucial for the design and modification of catalysts and for the in-depth understanding of catalyst selectivity and stability. Cobalt-based materials exhibit relatively high activity in some reactions, such as 5-hydroxymethylfurfural oxidation[25] and glycerol oxidation,[26,27] and can be used as dopants or co-catalysts to promote the activity of nickel-based catalysts. It is necessary to clarify the effect of cobalt doping on nickel-based catalysts and mechanisms, which will help to design better and modify the catalysts and to understand issues such as activity, selectivity, and stability.

Chi et al. prepared self-supported ultrathin NiCo layered double hydroxide (LDHs) electrodes as an anode for methanol electrooxidation reaction (MOR) to achieve a high formate production rate.[28] They revealed that ultrathin LDHs were beneficial for the formation of Ni^{3+} in hydroxides and introducing oxygen vacancy in NiCo-LDH could decrease the energy barrier of the rate-determining step for MOR. Hui et al. further found that interpolated phosphate in LDH can act as a proton transfer intermediate and effectively promote NOR.[29] In earlier studies, metal phosphates have displayed many academic interests and technological applications due to their unique chemical structure and reactivity for NOR.[30,31] In addition, because amorphous materials are rich in low-corded atoms and defects, they can provide sufficient catalytic active centers, which is widely concerned.[32,33]

Here, a series of cobalt-doped amorphous nickel phosphate materials (Co-NiP$_x$O$_y$/NF) were grown by electrodeposition on

J. Shen, C. Hong, Y. Qi, Y. Zhu
Key Laboratory for Ultrafine Materials of Ministry of Education
School of Materials Science and Engineering
East China University of Science and Technology
Shanghai 200237, China
H. Jiang, C. Li
Shanghai Engineering Research Center of Hierarchical Nanomaterials
School of Chemical Engineering
East China University of Science and Technology
Shanghai 200237, China
E-mail: jhlworld@ecust.edu.cn; czli@ecust.edu.cn

The ORCID identification number(s) for the author(s) of this article can be found under https://doi.org/10.1002/smll.202503950

DOI: 10.1002/smll.202503950

nickel foam and used as catalysts for NOR. It was found that the 10% cobalt-doped material (10Co-NiP_xO_y/NF) catalyzed MOR with a 227 mV decrease in the applied potential required to reach a current density of 200 mA cm^{-2} compared with that of OER, and the Faraday efficiencies of the formate products during constant-current electrolysis at current densities of 20–250 mA cm^{-2} were above 90%, and the catalysts showed no degradation of performance originating from their own factors during the 120 h electrolysis process. With the elevated cobalt doping, a clear separation of the catalyst oxidation process from the MOR was found, implying that cobalt doping significantly affects the activity of the sites formed by the oxidation of the catalysts. This change is clearly associated with a change in the catalytic mechanism. For this purpose, we revealed the reaction mechanism of the catalysts and the effect of cobalt doping on the nickel-based catalysts by impedance spectroscopy relaxation time distribution analysis, potential-dependent in situ Raman spectroscopy, time-dependent Raman spectroscopy, and open-circuit potential test. We find that MOR on 10Co-NiP_xO_y/NF follows a dual mechanism involving hydrogen vacancy oxygen grabbing and electrophilic OH^* species. Density functional theory (DFT) calculations indicate that the introduction of Co reduces the reaction activation energy and enhances the catalytic activity by optimizing the intermediate adsorption energy. Based on the insights into the mechanism, further catalyst design ideas for different substrates were proposed.

2. Results and Discussion

2.1. Catalyst Characterization

A series of cobalt-doped amorphous nickel phosphate materials (denoted as *m*CoNiPxOy/NF) were grown by electrodeposition on nickel foam deposition (**Figure 1a**). As shown in Figure 1b–d for the scanning electron microscopy (SEM) and transmission electron microscope (TEM) characterization of 10Co-NiP_xO_y/NF, 10Co-NiP_xO_y/NF exhibits an agglomerated spherical particle structure and amorphous state. Scanning TEM with energy dispersive X-ray (STEM-EDX) showed a uniform distribution of Ni, Co, P, and O elements on the spherical particles, in Figure 1e. Samples with different Co contents also show a similar agglomerated spherical particle structure (Figure S1, Supporting Information). For CoP_xO_y/NF, the surface exhibits more pronounced pore structures. Table S1 (Supporting Information) presents the content of each element in different samples. It can be seen that the stoichiometric ratios of Ni and Co elements in the actual material do not differ much from the feed ratios.

In the X-ray photoelectron spectroscopy (XPS) of 10Co-NiP_xO_y/NF (**Figure 2**), the peaks at 856.9 and 874.7 eV are attributed to Ni $2p_{3/2}$ and Ni $2p_{1/2}$, respectively, and their higher binding energies are consistent with the chemical state of nickel in nickel phosphates.[34,35] The 786.0 and 789.5 eV peaks are attributed to the satellite peaks of Co^{2+} and Co^{3+}, respectively. The firm Co^{2+} satellite peaks indicate that Co^{2+} is dominant on the surface of the catalyst, and the presence of Co^{3+} may be related to the disordered coordination in the amorphous structure of the catalyst. The peaks at 529.8, 531.6, and 533.1 eV are attributed to lattice oxygen, oxygen in phosphate, and adsorbed oxygen on the material surface, respectively. The peaks at 133.5 and 134.3 eV in the P 2*p* spectrum are attributed to P $2p_{3/2}$ and P $2p_{1/2}$ in phosphate, respectively. Other cobalt-doped nickel phosphate samples with different levels of cobalt exhibit the same XPS characteristics (Figure S2, Supporting Information). NiP_xO_y/NF showed multiple Raman peaks at 434.1, 575.2, 961.2, and 1060.0 cm^{-1}, which corresponded to the PO_4^{3-} symmetric bending vibration (υ_2), asymmetric bending vibration (υ_4), symmetric stretching vibration (υ_1), and asymmetric stretching vibration (υ_3), respectively. The local bonding configuration of the phosphate group (PO_4^{3-}) was not significantly altered under low-concentration cobalt doping conditions (Figure S3, Supporting Information).

2.2. Electrocatalytic Properties

First, we compared the MOR performance of different samples. As shown in **Figure 3a**, it can be found that *m*Co-NiP_xO_y/NF significantly outperforms the nickel foam substrate, NiP_xO_y/NF, and CoP_xO_y/NF. For *m*Co-NiP_xO_y/NF, as the content of doped cobalt is elevated (m increases), the applied potential required in the low current density range of the linear sweep voltammetry (LSV) curve decreases. In contrast, the applied potential required to reach high current densities (> 250 mA cm^{-2}) does not decrease significantly or even increase. In addition, oxidation peaks can be observed in the low potential range (1.15–1.30 V) when the cobalt content is high, and we will discuss the cause of this phenomenon in more detail later, which is linked to the reaction mechanism of the catalyst. The Tafel plot (Figure 3b) shows that 10Co-NiP_xO_y/NF exhibits the lowest Tafel slope (23.4 mV dec^{-1}), which is higher than that of the cobalt-free doped NiP_xO_y/NF, suggesting that cobalt doping can improve the reaction kinetics of nickel phosphate catalyzed MOR. However, as the cobalt doping ratio increases, the Tafel slope begins to decrease, indicating that too much cobalt doping seems detrimental to MOR. CoP_xO_y/NF exhibits the highest Tafel slope, suggesting that the catalytic kinetics of CoP_xO_y/NF for MOR is poor.

As shown in Figures S4 and S5 (Supporting Information), after evaluating the C_{dl} of each sample, it was found that NiP_xO_y/NF exhibited the lowest C_{dl}. In contrast, CoP_xO_y/NF exhibited the highest C_{dl}, which may be related to the rough and porous structure of the CoP_xO_y/NF surface. The overall C_{dl} of *m*Co-NiP_xO_y/NF shows an increasing trend with increasing cobalt content. We normalized the catalytic activity of each sample by electrochemical active surface area (ECSA) and found that 10Co-NiP_xO_y/NF exhibited the highest activity (Figure S6, Supporting Information). As shown in Figure 3c, 10% cobalt doping significantly reduces the applied potential required for OER and MOR to reach the same current density compared to cobalt-free nickel phosphate. For 10Co-NiP_xO_y/NF, the applied potential for MOR catalyzed by 10Co-NiPxOy/NF to reach a current density of 200 mA cm^{-2} decreased by 227 mV compared with that of OER, which dramatically reduces the potential of the anodic reaction. 10Co-NiP_xO_y/NF also exhibited high selectivity for formate products, with Faraday efficiencies (FE) above 90% for formate products during constant-current electrolysis at current densities from 20–250 mA cm^{-2} (Figure S7, Supporting Information). Among the nickel foam self-supported nickel-based catalysts reported in recent years, 10Co-NiP_xO_y/NF also performs well (Figure 3d; Table S2, Supporting Information). Compared

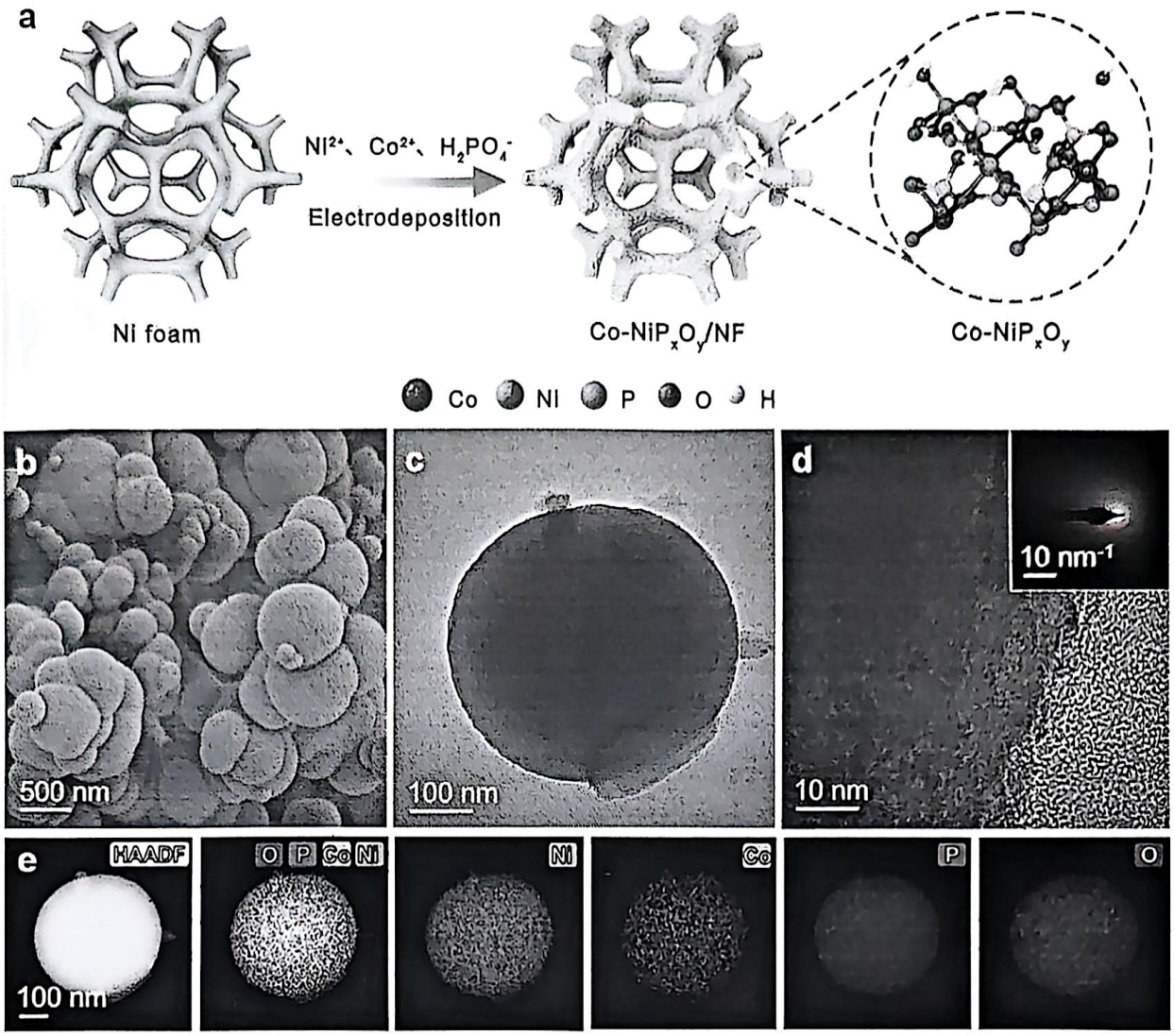

Figure 1. a) Schematic diagram showing the synthesis process of Co-NiP_xO_y/NF. b) SEM image of the prepared 10Co-NiP_xO_y/NF catalyst. c) TEM image of the prepared 10Co-NiP_xO_y/NF catalyst. d) HRTEM image of the prepared 10Co-NiP_xO_y/NF catalyst (inset shows SAED spectrum). e) HADDF-STEM image of the prepared 10Co-NiP_xO_y/NF catalyst. f–j) elemental mappings of 10Co-NiP_xO_y/NF catalyst.

with previously reported Ni, NiP_x, NiMn, and NiCo-derived catalysts, the 10Co-NiP_xO_y/NF electrode requires a potential of only 1.370 V at 5 mA cm_{ECSA}^{-2} in 1 M KOH + 1 M MeOH, exhibiting a decrease of 14–26 mV relative to Ni-NF-Af, MoO_3/$Ni(OH)_2$, and NiP_x-R. Additionally, this electrode ranks first at 2 mA cm_{ECSA}^{-2} with a low potential of 1.348 V. 10Co-NiP_xO_y/NF also showed good stability, as shown in Figure 3e, during the electrolysis at 100 mA cm^{-2} for 120 h, the electrolyte was changed every 12 h to exclude the performance degradation caused by the decrease of KOH concentration due to the rapid depletion of KOH. It can be seen that there is almost no degradation of the catalyst activity before and after 120 h of electrolysis. After long-term stability testing, the 10Co-NiP_xO_y/NF catalyst retained its agglomerated spherical particle morphology(Figure S8, Supporting Information). As shown in Figure S9 (Supporting Information), the Ni 2*p* spectrum obtained from the catalyst surface after stability testing revealed that the binding energy of Ni $2p_{3/2}$ shifted from the initial value of 856.9 to 855.6 eV. This negative shift of the main peak indicates a reduction in the average oxidation state of Ni, corresponding to an increase in electron density. Additionally, the satellite peak position for Co^{2+} moved from 786.0 to 785.7 eV, and that for Co^{3+} shifted from 789.5 to 788.9 eV, demonstrating that partial reversible reduction of Co^{3+} species occurred during prolonged methanol oxidation. In the P 2*p* spectra, the disappearance of surface phosphorus signals was observed. These surface characteristics remained essentially consistent with the state after MOR, demonstrating the long-term structural stability of the catalyst.

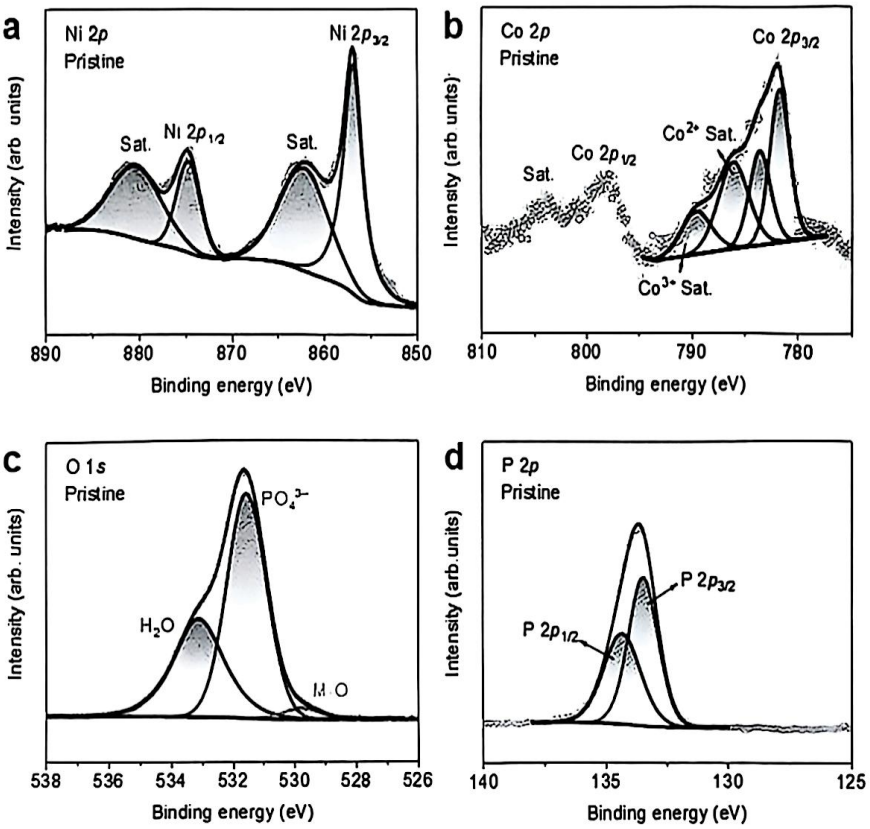

Figure 2. XPS spectra of 10Co-NiP_xO_y/NF, a) Ni 2*p* spectrum, b) Co 2*p* spectrum, c) O 1*s* spectrum, and (d) P 2*p* spectrum.

2.3. Analysis of Electrochemical Processes

Nickel foam substrates have poor catalytic performance due to the lack of electroactive components on the surface. As shown in Figure S10 (Supporting Information), the Ni^{3+}-O vibrations of nickel foam during the MOR process are weak, indicating that it is difficult to form a high-valent nickel surface on the nickel foam surface when methanol is present. Due to the lack of high-valent nickel adsorption sites, the formation of OH^* is hindered. At this point, the MOR is more likely to follow the hydrogen vacuolar oxygen-robbing mechanism.[36] For the OER process on nickel foam, the Bode plot after 1.36 V exhibits a typical dual-process feature, with the response biased toward the high-frequency side corresponding to the catalyst's electro-oxidation process and the response biased toward the low-frequency side corresponding to the OER (Figure S11a, Supporting Information). For the nickel foam substrate, it can be seen that a high-frequency reaction is present, which is related to the lack of electrically active material on the nickel foam surface, which is difficult to oxidize. As the potential increases, it can be seen that the low-frequency response related to OER almost disappears due to the difficulty in oxidizing the catalyst, resulting in a very high percentage of the impedance of the catalyst oxidation process. In contrast, the percentage of OER in the total reaction impedance decreases with the potential increase and is eventually no longer significantly reflected in the impedance spectrum. From Figure S11a (Supporting Information), it can be observed that the response frequency of the bilayer capacitance and the catalyst's own electro-oxidation is low, probably due to the large capacitance caused by the vast surface area of the nickel foam. For the MOR process on the Ni foam substrate (Figure S11b, Supporting Information), it can be seen that the MOR occurs in the high-frequency region, which is consistent with the conclusion derived from the in situ Raman spectroscopy, suggesting that the MOR on the Ni foam substrate mainly follows the hydrogen vacuolar oxygen-hydrogen grabbing mechanism.

Based on the study of the electrochemical impedance spectroscopy (EIS) characteristics of the nickel foam substrate, we further analyze the impedance spectral characteristics of 10Co-NiP_xO_y/NF, which exhibits good catalytic activity for MOR. As shown in **Figure 4a–d**, it can be seen that 10Co-NiP_xO_y/NF exhibits strong Ni^{3+}-O vibrations in both OER and MOR processes, indicating the oxidation of the catalyst and the formation of high valence surfaces, which is related to the surface nature of the amorphous material that is prone to oxidation, as well as the strong charge transfer capability between the material and the nickel foam substrate. However, the appearance of the strong Ni^{3+}-O vibrational signal in the MOR process is significantly later than that of the OER, indicating that there is an inhibitory effect of the presence of methanol on the electrooxidation of the catalyst, which is brought about by the filling of hydrogen vacancies formed by hydroxyl deprotonation on the catalyst surface by methanol. As shown in Figure S12 (Supporting Information), with increasing cobalt content, the intensity of the Ni

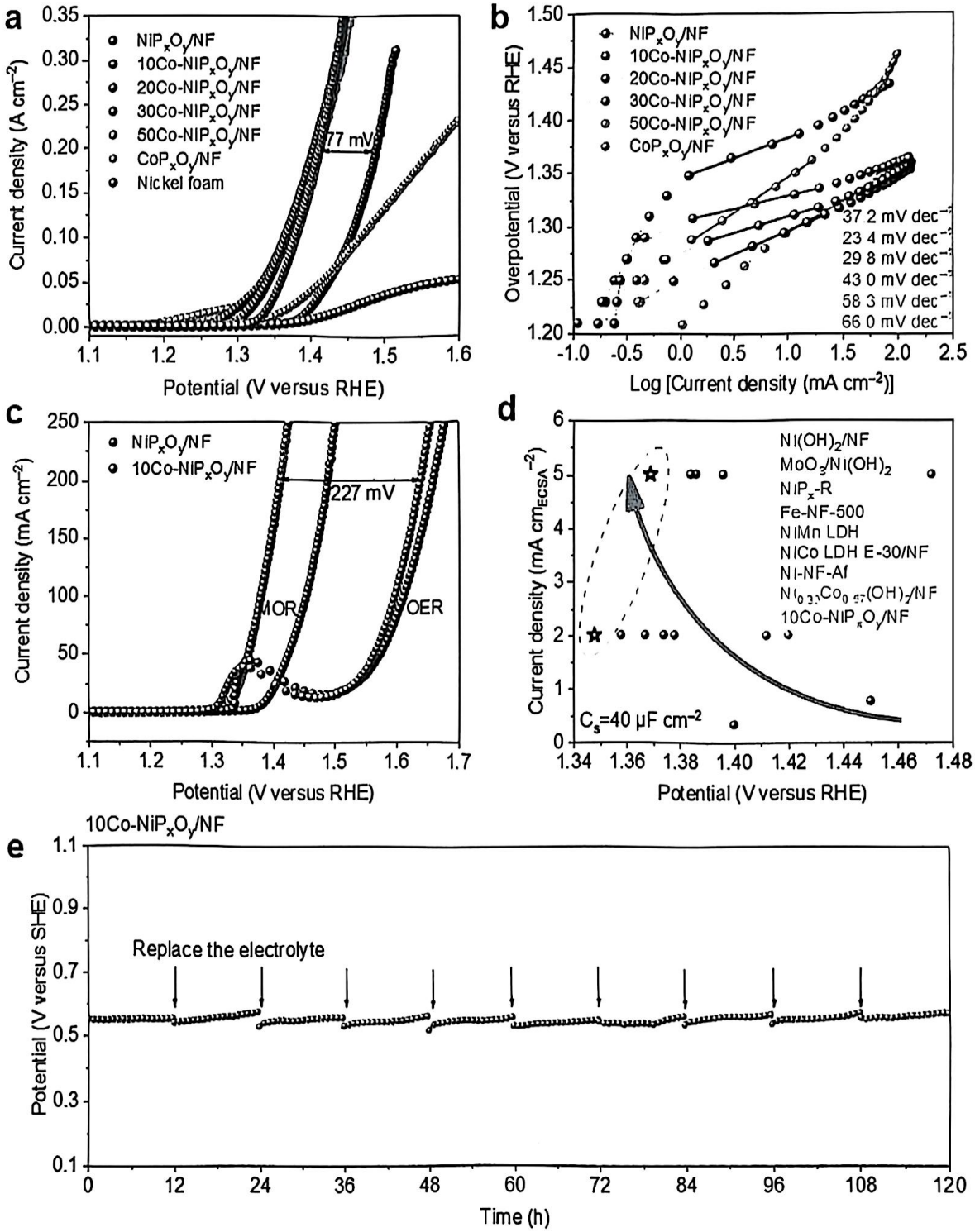

Figure 3. a) LSV curves of samples in 1 M KOH + 1 M MeOH (methanol) electrolyte. b) Tafel plots of samples in 1 M KOH + 1 M MeOH electrolyte. c) LSV curves of NiP$_x$O$_y$/NF and 10Co-NiP$_x$O$_y$/NF at MOR vs. OER. d) Comparison of the performance of 10Co-NiP$_x$O$_y$/NF with recently reported materials. Related references are in the Supporting Information. e) Chronopotential curves of 10Co-NiP$_x$O$_y$/NF at 100 mA cm^{-2} in 1 M KOH + 1 M MeOH electrolyte.

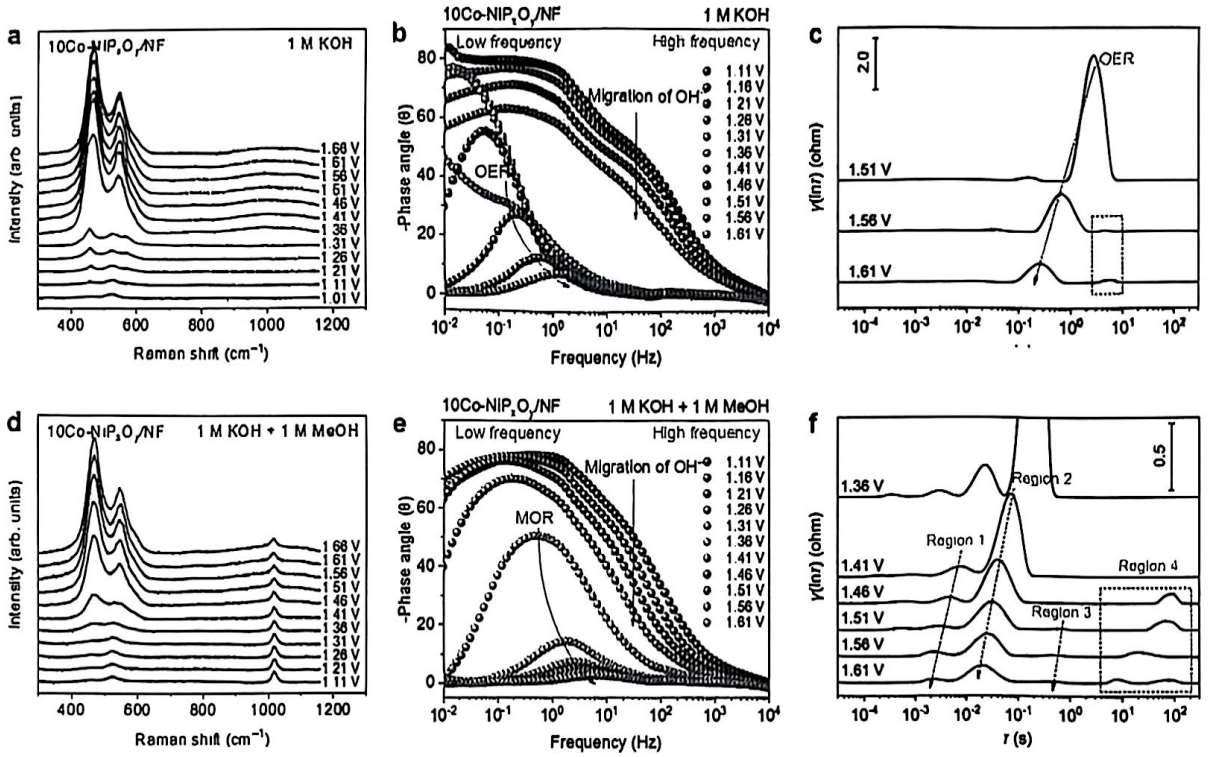

Figure 4. a) In situ Raman spectra of 10Co-NiP$_x$O$_y$/NF collected in 1 M KOH electrolyte. b) Bode plots of 10Co-NiP$_x$O$_y$/NF in 1 M KOH electrolyte. c) DRT plot of EIS for OER process on 10Co-NiP$_x$O$_y$/NF catalysts. d) In situ Raman spectra of 10Co-NiP$_x$O$_y$/NF collected in 1 M KOH + 1 M MeOH electrolyte. e) Bode plots of 10Co-NiP$_x$O$_y$/NF in 1 M KOH + 1 M MeOH electrolyte. f) DRT plot of EIS for MOR process on 10Co-NiP$_x$O$_y$/NF catalysts.

2*p* peaks gradually decreased, while that of the Co 2*p* peaks progressively increased. Under alkaline oxygen evolution reaction conditions, the 10Co-NiP$_x$O$_y$/NF catalyst underwent significant surface electronic reconstruction involving phosphide re-oxidation.[35] Specifically, the Ni $2p_{3/2}$ and Ni $2p_{1/2}$ peaks exhibited an overall negative shift of ≈1.3–1.5 eV (from 856.9 to 855.6 eV and from 874.7 to 873.2 eV, respectively). Concurrently, the satellite peak of Co^{2+} shifted markedly from 786.0 to 784.1 eV, indicating a reduced charge transfer energy for cobalt, while the satellite peak of Co^{3+} shifted slightly upward, corroborating the occurrence of localized oxidation. After MOR, the positions of the Ni $2p_{3/2}$ and Ni $2p_{1/2}$ peaks in the XPS spectra shifted from 856.9 to 856.4 eV and from 874.7 to 874.0 eV, respectively. This distinct negative shift of the Ni 2*p* main peaks indicates a partial reduction of Ni^{3+} back to Ni^{2+}. Furthermore, the satellite peak of Co^{2+} showed a slight upward shift, whereas that of Co^{3+} shifted slightly downward. The negligible movement of Co satellite peaks demonstrates only a minor electronic buffering effect. The XPS of 10Co-NiP$_x$O$_y$/NF after OER reveals a large amount of lattice oxygen on the catalyst surface, and cobalt also exhibits +3 valence. The chemical state of the catalyst surface after MOR is basically the same as that of the unreacted catalyst after soaking in the electrolyte, which also proves that the methanol can supply hydrogen atoms to the hydrogen vacancy oxygen and thus inhibit the catalyst's transition to the high-valent oxidized surface to some extent. At high potentials, the catalyst deprotonates faster than the methanol fills the hydrogen vacancies, and the catalyst oxidizes and exhibits a strong Ni^{3+}-O vibrational signal. 10Co-NiP$_x$O$_y$/NF also suffers from the absence of high-frequency response in the impedance spectrum of the OER process (Figure 4b), suggesting that the nickel foam substrate greatly contributes to the electrooxidation process of the catalyst itself. This indicates that the nickel foam substrate greatly facilitated the electrooxidation process of the catalyst itself. As shown in Figure 4e, the response frequency of MOR was significantly higher than that of the OER process and lower than that of MOR on Ni foam substrate, which indicated that the catalytic mechanism of MOR on 10Co-NiP$_x$O$_y$/NF was between the hydrogen vacancy oxygen grabbing mechanism and the adsorption of oxygen-containing species.

In order to characterize the individual processes more intuitively, we further analyzed the impedance spectra in terms of distribution relaxation time (DRT). Figure 4f shows the DRT plot of 10Co-NiP$_x$O$_y$/NF in 1 M KOH + 1 M MeOH electrolyte. After reaching the MOR starting potential, there are multiple peaks in the DRT plot, representing the presence of multiple processes, which are difficult to visually observe by conventional impedance analysis and difficult to visualize by traditional analysis of impedance empirical methods. Here, we divide the major peaks in the DRT plot into four regions. For the peaks in Region 1 and Region 2, it can be seen that as the potential increases, the peak intensities of the peaks in these two regions decrease and shift toward higher frequencies, indicating that these two processes are gradually favored as the potential increases. DRT

plots tend to present major processes.[37] The peaks in Region 2 clearly represent the main process, i.e., the MOR process. The peaks in Region 1 have higher frequencies and smaller time constants than those in Region 2, and we believe that Region 1 is related to the electrooxidation process of the catalyst. If the hydrogen vacancy oxygen formed by the catalyst deprotonation is sufficiently reactive, the MOR process will also occur due to hydrogen grabbing by the hydrogen vacancy oxygen. The MOR in Region 2, which is slightly lower in frequency, is more likely to be catalyzed by surface electrophilic oxygenated species. After reaching 1.51 V, a new peak begins to appear in Region 3, and this potential interval is highly compatible with that of the onset of OER and, therefore, likely represents the onset of the OER process.

From the DRT plot of 10Co-NiP_xO_y/NF in 1 M KOH electrolyte shown in Figure 4c, it can be seen that the time constants and frequencies of the peaks associated with the OER process and Region 3 fit highly, which verifies our conjecture. It can be seen that the peak representing the OER process in Region 3 is not strong, which indicates that OER is not the main process of anodic reaction. As the potential of the MOR process increases, multiple peaks begin to appear in Region 4, and these low-frequency peaks are associated with the diffusion of material. In the high potential range of Figure 4c, we also observe similar low-frequency peaks ≈5 s. Therefore, we hypothesize that the peaks ≈5 s represent OH-diffusion, which affects both OER and MOR processes. The peaks ≈80 s in the MOR process can thus be assigned to the methanol diffusion process, which is related to the rapid consumption of methanol on the electrode surface at high potentials. The DRT plots of NiP_xO_y/NF in the MOR process show characteristics consistent with those of 10Co-NiPxOy/NF, where the peaks in Region 1 are significantly weaker than those in Region 2, suggesting that there is little obstruction to the catalyst's electrooxidation, while the opposite is true for powdered NiP_xO_y (Figure S13, Supporting Information). The opposite is true for powdered NiP_xO_y (Figure S14, Supporting Information). The frequencies of the two peaks P1 (catalyst oxidation as well as directly associated MOR) and P2 (electrophilic OH^*-associated MOR) associated with MOR during MOR of powdered NiP_xO_y are about an order of magnitude higher than those of NiP_xO_y/NF. They are stronger at peak P1 than at peak P2 as the potential rises. The intensity of P1 is higher due to the poor conductivity of the disordered nickel hydroxide transformed by NiP_xO_y in the electrolyte, the difficulty of electrooxidation of the catalyst itself, and the oxidation process of the catalyst, which is the main bottleneck limiting the anodic reaction as well as the main process occurring. Due to the limitation of catalyst electrooxidation, it is challenging to form high-valent nickel surfaces on a large scale, and there is a lack of active sites for OER, so the peaks related to OER were not observed. Due to the low catalytic activity and slow consumption of reactants, the peaks related to its diffusive mass-transfer process appear at a higher potential of 1.66 V. From the above analysis, it can be seen that the DRT method can divide the catalyst oxidation process, the main reaction process, the competitive reaction process and the diffusive mass transfer process more clearly, which helps to understand the emergence and changes of each process in depth.

2.4. In-Depth Knowledge of Catalytic Mechanisms

In ESI analysis, we found that the MOR mechanism on NiP_xO_y/NF and 10Co-NiP_xO_y/NF is likely to be a composite catalytic mechanism involving both hydrogen vacancy oxygen and electrophilic OH^* species. The MOR in the hydrogen vacancy oxygen mechanism is directly related to the catalyst's own electrooxidation. In the electrophilic OH^* mechanism, the MOR is indirectly related to the catalyst's own electro-oxidation, and there is a certain separation between the catalyst oxidation current and the catalytic current. However, we found that even in the presence of 1 M high methanol concentration, the oxidation current of the catalyst seems to have a tendency to be independent of the MOR current (Figure 3a,b), and to visualize this phenomenon more, we compared the step cyclic voltammetry (SCV) curves with the LSV curves (Figure S15, Supporting Information). Steady-state SCV testing allows for the circumvention of charge/ discharge currents other than reaction currents, which include those contributed by catalyst oxidation. The LSV and SCV curves for 10Co-NiP_xO_y/NF are almost coincident, and as the cobalt content increases, the catalyst oxidation current becomes more and more obvious in the LSV curve. This implies that the oxidation process of the catalyst is separated from the MOR process as the cobalt content increases, which also means that the interaction between methanol and hydrogen vacancy oxygen becomes more difficult.

During the MOR reaction, active sites or active species are formed on the catalyst surface, and no new active sites or active species are generated when the potential is no longer applied. At this time, the reaction substrate will still interact with the remaining active sites or active species on the catalyst surface, thus causing a change in the catalyst surface, which will result in a change in the open-circuit potential of the catalyst. When the active sites or active species on the catalyst surface are depleted, the catalyst surface remains stable, and the open-circuit potential no longer changes significantly. Therefore, we can form active sites or active species on the catalyst surface by applying a short-time constant potential and clarify the reaction between the reaction substrate and the catalytic sites or catalytic species according to the change of the open-circuit potential with time.

We also take 10Co-NiP_xO_y/NF as an example, as shown in Figure 5a, immediately after applying a constant potential of 1.51 V for 15 s, the open circuit was kept open, and the change in open circuit potential with time was recorded. In the 1 M KOH electrolyte (red dotted line), the open-circuit potential decreased slightly after the constant potential and gradually stabilized around ≈1.3 V. The open-circuit potential was then adjusted to a constant potential of 1.51 V at 900 s. The open-circuit potential was then adjusted to a constant potential of 1.3 V. When methanol was added to the standing 1 M KOH electrolyte at 900 s (in the amount that would form a 1 M concentration after complete dissolution), the open-circuit potential began to drop significantly and stabilized at ≈1600 s. Therefore, it can be concluded that the significant change in open-circuit potential is related to the depletion of active sites or active species on the catalyst surface by methanol. In the 1 M KOH + 1 M MeOH electrolyte (purple dotted line), the open-circuit potential exhibits a rapid decrease after constant potential and stabilizes and remains ≈0.5 V at ≈340 s. In the 1 M KOH + 1 M MeOH electrolyte (purple dotted

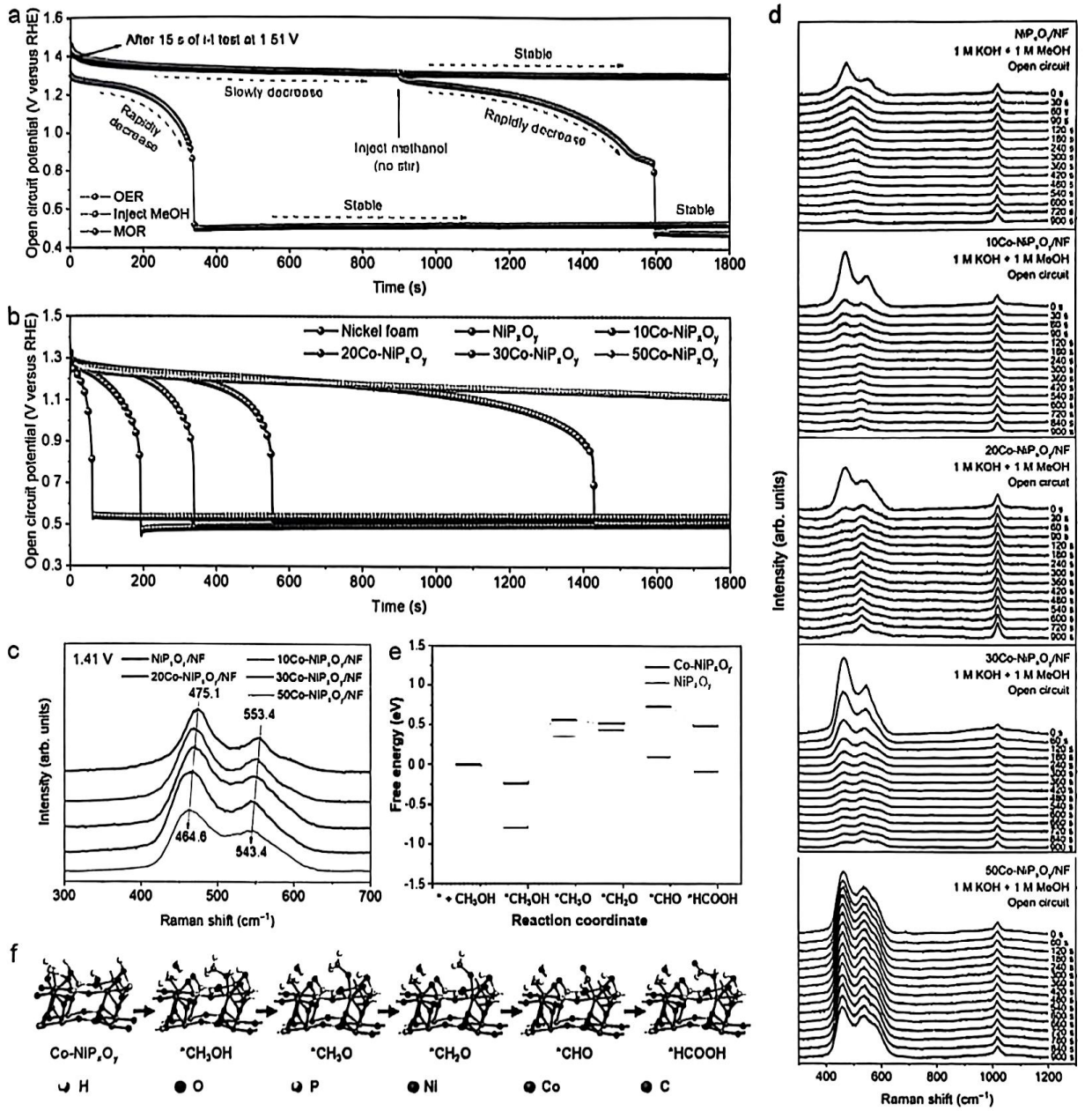

Figure 5. a) The effect of the presence or absence of methanol on the open circuit potential. b) The variation of open circuit potential of different samples over time after applying a constant potential of 1.51 V for 15 s in 1 M KOH + 1 M MeOH electrolyte. c) Comparison of Ni^{3+}-O vibration signals of different samples. d) Time-dependent Raman spectra of different samples in an open circuit state after applying a constant potential of 1.51 V for 15 s in 1 M KOH + 1 M MeOH electrolyte. e) Flow diagram of Co-NiP_xO_y and NiP_xO_y catalyzed Gibbs free energy. f) The structures of various MOR intermediates on Co-NiP_xO_y.

line), the open-circuit potential decreases rapidly and stabilizes ≈0.5 V after a slight decrease. In the 1 M KOH electrolyte (blue dotted line), the open-circuit potential stabilizes after a slight drop in the first period, which is due to the lack of strong KOH in the electrolyte. This is due to the lack of strong nucleophilic substrates in the electrolyte, and the Co-NiOOH formed by oxidation of the catalyst during the OER process can stably exist, so the open-circuit potential remains stable and maintains at a high level of ≈1.3 V. The open-circuit potential of the catalyst in the 1 M KOH electrolyte (blue dotted line) remains stable after a slight drop in the early stage.

We further investigated the trend of open-circuit potential with time after constant potential for other samples, as shown in Figure 5b. For nickel foam, the open-circuit potential decreased

rapidly, minimized at ≈60 s, and remained stable. Since it is difficult to oxidize the surface of nickel foam to form a high-valent nickel surface, and there is no large amount of hydrogen vacancy oxygen and OH^* species present on the surface, its open-circuit potential can be rapidly decreased and stabilized. As the amount of cobalt doping in nickel phosphate is elevated, it can be noticed that the time required for the open-circuit potential to decrease and reach stability grows progressively, which implies that the structure of the high-valent oxides formed by the catalyst oxidation is more stable. We further demonstrate this point by Raman spectroscopy. Figure S16 (Supporting Information) shows the in situ Raman spectra of different cobalt-doped samples for the MOR process. It can be seen that the vibrational signals of Ni^{3+}-O appeared in the MOR process, whether it was 10Co-NiP_xO_y/NF, 20Co-NiP_xO_y/NF, 30Co-NiP_xO_y/NF or 50Co-NiP_xO_y/NF. The difference is the potential at which the Ni^{3+}-O vibration signal appears. The higher the cobalt content, the higher the intensity of the Ni^{3+}-O vibration signal at the very beginning, which means that the hydrogen vacancy oxygen formed by the deprotonation of the hydroxyl group on the surface of the catalyst during the electrooxidation is more likely to accumulate and induce the catalyst to transform into a hydroxyl oxide structure.

The post-reaction XPS shows that 30Co-NiP_xO_y/NF (Figure S17, Supporting Information) and 50Co-NiP_xO_y/NF (Figure S18, Supporting Information) have a large amount of lattice oxygen on the surface after MOR and the surface cobalt mainly exhibits +3 valence, and the characteristics of post-MOR XPS are similar to that after OER, which also proves that the accumulation of hydroxide vacancy oxygen is easy to accumulate under high cobalt content. The accumulation of hydrogen vacancy oxygen may originate from the low substrate concentration, the substrate's reactivity, and the catalyst's nature. In the case discussed, where the substrates are all methanol and the concentrations are uniformly high at 1 M, the large accumulation of hydrogen vacancy oxygen is obviously closely related to the nature of the catalyst itself, as the cobalt content increases, the ability of the hydrogen vacancy oxygen formed by hydroxyl deprotonation on the surface of the catalyst to capture hydrogen atoms in the methanol molecule decreases. Figure 5c shows that the bending and stretching vibrational modes of Ni^{3+}-O are gradually red-shifted with elevated cobalt content, suggesting that the introduction of cobalt significantly affects the electronic structure of nickel, which may lead to a decrease in the electron-deficient nature of the hydrogen vacancy oxygen and a subsequent decrease in the ability to capture hydrogen atoms.

Figure 5d illustrates the time-dependent Raman spectra of different samples at different open-circuit durations after 15 s 1.51 V constant potential. The bending vibration and stretching vibration signals of Ni^{3+}-O of NiP_xO_y/NF disappear rapidly after constant potential, indicating that the hydrogen vacancies on the high-valent nickel oxides are filled rapidly after the oxidation of the catalysts, resulting in the reduction of the high-valent surface of the catalysts. The length of time required for the disappearance of the Ni^{3+}-O vibration signal gradually increases as the cobalt content is elevated. For 50Co-NiP_xO_y/NF, there is no significant change in the intensity of Ni^{3+}-O vibrational signals during the observation of 900 s. This indicates that the catalytic reactivity of 50Co-NiP_xO_y/NF in the MOR process toward methanol oxidation is very low. Its own hydrogen vacancies are difficult to fill up by the hydrogen in the methanol molecule, and thus, the structure can exist in a relatively stable manner. It can be seen that the results of Raman spectroscopy are consistent with the trend of the open-circuit potential with time.

So far, in the previous performance tests, shown in Figure S19 (Supporting Information), we learned that the 10Co-NiP_xO_y/NF electrode exhibited an operating potential of only 1.370 V vs. RHE, which is 61 mV lower than that of the cobalt-free sample. Correspondingly, its Tafel slope significantly decreased from 37.2 to 23.4 mV dec^{-1}, demonstrating effective charge compensation while maintaining a high density of active Ni sites. Consequently, oxygen species at hydrogen vacancies readily acquire electrons, achieving synergistic catalysis. The 20Co-NiP_xO_y/NF catalyst displayed a slightly higher operating potential (1.373 V) and Tafel slope (29.8 mV dec^{-1}) than the 10Co sample, yet it still outperformed both pure Ni and catalysts with higher cobalt loadings. As the cobalt content increased further, catalytic performance deteriorated; for instance, the operating potentials of the 30Co and 50Co samples rose to 1.378 V, with their Tafel slopes increasing to 43 and 58.3 mV dec^{-1}, respectively. Pure CoP_xO_y/NF exhibited an even higher potential of 1.587 V and a Tafel slope of 66 mV dec^{-1}. Elevated cobalt content facilitated earlier oxidation of Ni sites but simultaneously weakened the electrophilicity of the oxygen species formed at neighboring hydrogen vacancies. Under these conditions, the MOR mechanism involving electrophilic OH^* species became dominant. With the progressive depletion of unoxidized Ni sites and cobalt sites, oxidation of remaining Ni sites less influenced by cobalt became increasingly dominant, thus hindering the electro-oxidation efficiency of the catalyst.

It can be seen in Figure 5e that the free energy of the methanol adsorption state is below 0 eV for both catalysts Co-NiP_xO_y and NiP_xO_y. The free energy of the methanol adsorption state of Co-NiP_xO_y is slightly lower than that of NiP_xO_y. Co-NiP_xO_y may have a more robust adsorption capacity, resulting in lower free energy of its methanol adsorption state. Methanol undergoes a dehydrogenation reaction in the presence of a catalyst, removing one hydrogen atom to form $^*CH_3O$. This process involves overcoming specific energy barriers so the free energy rises. Co-NiP_xO_y catalysts may be more conducive to lowering the activation energy of this reaction so that the energy rise is relatively small. The structures of various MOR intermediates on Co-NiP_xO_y are shown in Figure 5f. Methanol adsorbs via its oxygen atom onto Ni^{3+}-OH sites, forming $*CH_3OH$ species. Assisted by surface hydroxyl groups, the α-H is abstracted, generating $^*CH_3O$. Subsequently, $^*CH_3O$ undergoes further dehydrogenation to form $^*CH_2O$, which is then converted to $^*CHO$ through β-H abstraction. The adjacent OH^- then attacks $^*CHO$, forming an $^*HCOOH$ complex. Among these steps, the initial deprotonation from $^*CH_3OH$ to $^*CH_3O$ exhibits the highest adsorption-free energy, thus being identified as the rate-determining step for the MOR. Notably, the Co-NiP_xO_y catalyst presents a substantially lower energy barrier than the undoped NiP_xO_y.

2.5. Nuclear Oxidation Properties of Different Substrates

We chose ethylene glycol, glycerol, and furfural as reaction substrates to demonstrate that cobalt doping indeed leads to a decrease in the oxygen-deficient electronegativity of the hydrogen

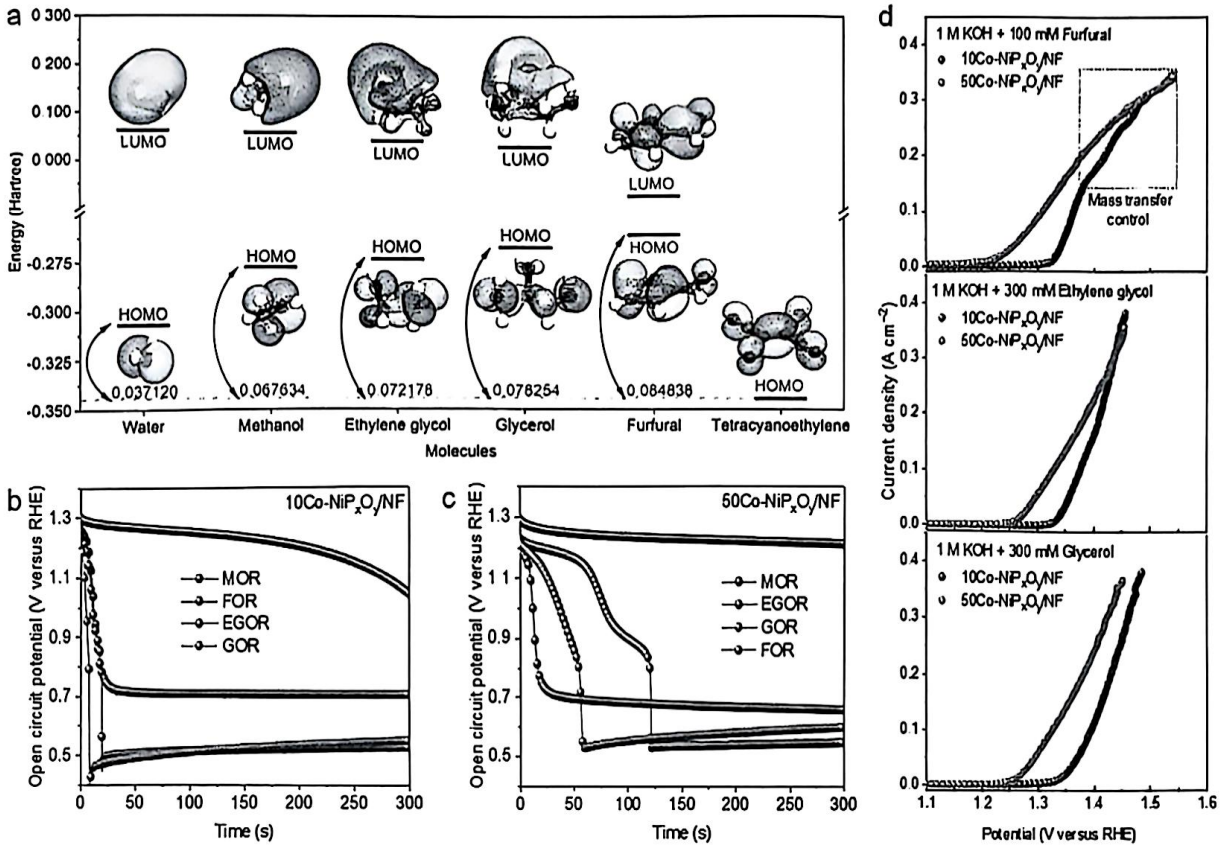

Figure 6. a) HOMO/LUMO energy levels and nucleophilicity indices of different molecules. Changes in open circuit potential of 10Co-NiP_xO_y/NF (b) and 50Co-NiP_xO_y/NF (c) over time in electrolytes containing different substrates. d) Comparison of LSV curves of 10Co-NiP_xO_y/NF and 50Co-NiP_xO_y/NF in electrolytes containing different substrates.

vacancies. As shown in Figure 6a, the nucleophilicity indices of water, methanol, ethylene glycol, glycerol, and furfural are 0.037, 0.068, 0.072, 0.078 and 0.085 Hartree, indicating that their electron-donating ability increases in that order (electron-donating ability is not fully linked to nucleophilicity, factors such as spatial site resistance also significantly affect the actual nucleophilicity of the substrate). When furfural (100 mM), glycerol (300 mM), and ethylene glycol (300 mM) were used as the reaction substrates, the trends of the open-circuit potentials were significantly different compared to the methanol substrate. As shown in Figure 6b,c, we investigated the change of open-circuit potential with time after a short period of constant potential for 10Co-NiP_xO_y/NF and 50Co-NiP_xO_y/NF. The open-circuit potential decreases rapidly when the substrates are furfural, glycerol, and ethylene glycol, much faster than when methanol is the substrate. This suggests that the more electron-donating furfural, glycerol, and ethylene glycol can interact rapidly with hydrogen vacancy oxygen on the catalyst surface. Even with a cobalt content of ≈50%, furfural, glycerol, and ethylene glycol can consume the oxidation sites on the catalyst surface more efficiently than methanol, showing strong nucleophilicity. As shown in Figure S20 (Supporting Information), the characteristics of the oxidation peaks in the LSV curves of 50Co-NiP_xO_y/NF in electrolytes with 1 M KOH and containing different organic substrates also show significant differences. The LSV curves of the MOR process show a Ni^{2+} to Ni^{3+} oxidation peak. But this oxidation peak is not reflected in the LSV curves of ethylene glycol oxidation (EGOR), glycerol oxidation (GOR), and furfural oxidation (FOR), which coincide with Ni^{2+} to Ni^{3+} oxidation, suggesting that hydrogen vacancy oxygen can easily capture hydrogen atoms from these nucleophilic organic substrates. Methanol, which is less nucleophilic, does not readily supply hydrogen atoms to the hydrogen vacancy oxygen on 50Co-NiP_xO_y/NF but readily supplies hydrogen atoms to the hydrogen vacancy oxygen on 10Co-NiP_xO_y/NF. Furfural, glycerol, and ethylene glycol, which are more nucleophilic than methanol, readily provide hydrogen atoms to the hydrogen vacancy oxygen on 50Co-NiP_xO_y/NF, and these phenomena indicate that the electrophilicity of the hydrogen vacancy oxygen is decreased at high cobalt content.

While cobalt doping significantly reduces the Ni^{2+} to Ni^{3+} oxidation potential, it also reduces the electrophilicity of the hydrogen vacancy oxygen. When the substrate is not strongly nucleophilic, too much cobalt doping leads to difficulties in the hydrogen vacancy oxygen mechanism, and the catalytic mechanism mainly follows the electrophilic OH^* species mechanism, which leads to a significant reduction in the role of cobalt doping in lowering the reaction potential. When the substrate is more nucleophilic, the organic substrate can more easily attack and provide

hydrogen atoms to the less electrophilic hydrogen vacancy oxygen, at which time the oxidation reaction of the organic substrate can be fused with the catalyst electro-oxidation process to realize the decreased reaction potential. As shown in Figure 6d, the onset potentials of FOR, EGOR, and GOR on 50Co-NiP_xO_y/NF are all lower than 10Co-NiP_xO_y/NF, but the advantage of FOR and EGOR activity is no longer apparent at higher potentials. In the case of FOR, the reason is mainly due to substrate diffusion limitation that hinders the performance enhancement; in the case of EGOR, it is mainly due to insufficient nucleophilicity of the substrate. When the substrate concentration is high enough and nucleophilic enough, the performance on 50Co-NiP_xO_y/NF tends to be superior to that on 10Co-NiP_xO_y/NF, even at high current densities (such as GOR).

Compared with MOR, EGOR, GOR, and FOR differ in that these latter reactions involve C—C bond cleavage steps. When substrates contain more carbon atoms, higher cobalt content in the catalyst corresponds to increased current density, more closely adhering to the electrophilic OH^* catalytic mechanism. In alkaline media, at high cobalt contents, oxygen species associated with hydrogen vacancies cannot efficiently participate in C—C bond cleavage. Consequently, oxygen sites formed at hydrogen vacancies during electro-oxidation of the catalyst struggle to promptly abstract hydrogen atoms from substrates. This leads to the accumulation of oxidized structural states, thereby providing adsorption sites for electrophilic oxygen species. At this stage, electrophilic OH^* species formed on the catalyst surface act as the active catalytic species. Interaction of ethylene glycol molecules with electrophilic OH^* facilitates C—C bond cleavage, generating intermediates such as $^*CH_2OH$ and $^*COOH$, ultimately producing formate ions.[38] Similarly, glycerol undergoes sequential fragmentation of its three-carbon backbone into C_1 products (primarily formate ions).[39] Moreover, in the furfural oxidation reaction, electrophilic OH species can attack side-chain carbons to induce C—C bond cleavage.[40]

Recent theoretical studies have expanded the mechanistic understanding of MOR from a single-pathway process to a complex parallel reaction network. Zhu et al. first identified the synergistic correlation between the dynamic cycling of Ni^{3+}-OOH ↔ Ni^{2+}-OH and indirect oxidation of adsorbed CO intermediates (CO^*) on NiMn-LDH.[41] Tian et al. employed ^{18}O-labeled Raman spectroscopy to quantitatively elucidate how OH coverage on NiCo-OOH surfaces dynamically regulates the coupled reaction rates of direct α-H abstraction and CO-mediated pathways.[42] While most nickel-based catalysts predominantly follow the hydrogen vacancy mechanism, this study incorporates cobalt doping into the nickel-based catalyst, thereby activating nickel oxidation states and establishing synergy between the "hydrogen abstraction via oxygen at hydrogen vacancies" and "electrophilic OH^*" pathways. This cooperative mechanism significantly enhances the oxidation efficiency for multi-carbon substrates.

In addition, we found that for the same catalyst 50Co-NiP_xO_y/NF, the onset potentials of the different oxidation reactions were significantly different, with FOR having a lower onset potential than GOR and GOR having a slightly lower onset potential than EGOR and a significantly lower onset potential than MOR. For 10Co-NiP_xO_y/NF, there was not much difference in the onset potentials of the reactions. After cobalt is doped into the material, it affects the surrounding nickel sites to different degrees. According to the phenomenon that the higher the cobalt doping, the lower the oxidation potential from Ni^{2+} to Ni^{3+} and the weaker the electrophilicity of the hydrogen vacancy oxygen, we speculate that the nickel sites which are more affected by cobalt are more prone to oxidize earlier. Still, the electrophilicity of the hydrogen vacancy oxygen formed around them is weaker as well. The broadening of the Ni^{2+} to Ni^{3+} oxidation peaks upon elevated cobalt doping may be a visualization of this speculation (Figure S21, Supporting Information). Since each nickel site is not affected by cobalt to the same extent, the hydrogen vacancy oxygen generated at different potentials has different reactivity. Hydrogen vacancy oxygen formed at high potential is less influenced by cobalt. It is more electrophilic, which is more favorable for catalyzing the oxidation of the substrate with weaker nucleophilicity, so the substrates with different nucleophilicity will have the phenomenon of different starting potentials of the oxidation reaction. When the nucleophilicity of the substrate makes it difficult to match the electrophilicity of the hydrogen vacancy oxygen, the MOR mechanism involving electrophilic OH^* species becomes dominant, such as the MOR process on 50Co-NiP_xO_y/NF. As shown in Figure S22 (Supporting Information), with the increase of cobalt doping in nickel phosphate, the response frequency of MOR at 1.36 V gradually shifts to a lower frequency, and the time constant also increases, which also indicates that electrophilic OH^* species are involved in the MOR to a greater extent.

A large amount of cobalt-doped nickel-based powder materials often have poor stability in the process of organic oxidation reactions, and we have observed similar phenomena in many published studies.[43–45] In this study, we found that the nickel-cobalt interface material and cobalt-doped nickel-based material on the foam nickel collector electrode showed good long-term stability. As shown in Figure S23 (Supporting Information), even if the content of cobalt reaches ≈50%, there is no active attenuation due to its own factors in the long-term test of MOR (the decline in performance in each cycle is caused by the decrease in KOH concentration). We speculate that this is due to the rapid electrical oxidation process of the catalyst on the foam nickel. Compared with powder materials, more thorough oxidation can occur faster, complete the phase transformation to hydroxyl oxide, and reach a stable state. The active site occupies less, so the performance is more stable (Figure S24, Supporting Information). In the early stage of the constant current test, it can be seen that the potential increases rapidly from a low value, and the impedance spectrum also shows the phenomenon of high-frequency response missing, which confirms the rapid occurrence of catalyst oxidation on foam nickel.

3. Conclusion

In summary, we prepared a series of nickel foam-loaded cobalt-doped nickel phosphate materials (mCo-NiP_xO_y/NF) as catalysts for nucleophilic oxidation reactions by electrodeposition. 10Co-NiP_xO_y/NF exhibited good MOR activity and can be stabilized at a current density of 100 mA cm^{-2} for at least 120 h without self-induced performance degradation and also exhibited high selectivity (>90%) for formate products. Empirical and DRT analyses of in situ electrochemical impedance spectra revealed that MOR on 10Co-NiP_xO_y/NF follows a dual mechanism of

hydrogen vacancy oxygen grabbing and involvement of electrophilic OH^* species. DFT calculations indicate that the introduction of Co reduces the reaction activation energy and enhances the catalytic activity by optimizing the intermediate adsorption energy.It was further investigated and found that cobalt doping reduces the electrophilicity of the hydrogen vacancy oxygen sites formed by hydroxyl deprotonation on the catalyst surface by open-circuit potential testing technique as well as Raman spectroscopy. When the substrate is not highly nucleophilic, substantial cobalt doping is detrimental to the hydrogen vacancy oxygen-grabbing mechanism, and the catalytic mechanism is more favorable to the electrophilic OH^* species mechanism. The findings of the present work provide new ideas for the design of efficient catalysts for the oxidation reactions of different organic nucleophilic substrates.

Supporting Information

Supporting Information is available from the Wiley Online Library or from the author.

Acknowledgements

This work was supported by the National Natural Science Foundation of China (22178106, U24A20546, 22278136, U22B20143), the Science and Technology Commission of Shanghai Municipality (23ZR1416400, 22dz1205900), Program for Professor of Special Appointment (Eastern Scholar) at Shanghai Institutes of High Learning, and the Fundamental Research Funds for the Central Universities (222201718002).

Conflict of Interest

The authors declare no conflict of interest.

Author Contributions

J.S. contributed to writing through review and editing; C.H. was responsible for the original draft preparation; Y.Q. Conducted the investigation and contributed to the methodology and conceptualization; Y.Z. Provided supervision and developed software; H.J. participated in writing through review and editing; and C.L. contributed resources and secured funding acquisition.

Data Availability Statement

The data that support the findings of this study are available from the corresponding author upon reasonable request.

Keywords

amorphous state, catalytic mechanism, methanol oxidation reaction, nucleophile oxidation reaction

Received: March 28, 2025
Revised: May 22, 2025
Published online:

[1] S. Fawzy, A. I. Osman, J. Doran, D. W. Rooney, *Environ. Chem. Lett.* **2020**, *18*, 2069.
[2] F. Dawood, M. Anda, G. M. Shafiullah, *Int. J. Hydrogen Energy* **2020**, *45*, 3847.
[3] G. Nicoletti, N. Arcuri, G. Nicoletti, R. Bruno, *Energy Convers. Manage.* **2015**, *89*, 205.
[4] L. Zhang, C. Jia, F. Bai, W. Wang, S. An, K. Zhao, Z. Li, J. Li, H. Sun, *Fuel* **2024**, *355*, 129455.
[5] M. F. Lagadec, A. Grimaud, *Nat. Mater.* **2020**, *19*, 1140.
[6] N. Tenhumberg, K. Büker, *Chem. Ing. Tech.* **2020**, *92*, 1586.
[7] C. Dong, J. Zhou, X. Su, Y. Wang, X. Yang, Y. Zhu, H. Jiang, C. Li, *Chem. Eng. Sci.* **2022**, *252*, 117270.
[8] X. Ren, T. Wu, Y. Sun, Y. Li, G. Xian, X. Liu, C. Shen, J. Gracia, H.-J. Gao, H. Yang, Z. J. Xu, *Nat. Commun.* **2021**, *12*, 2608.
[9] Y. Wen, C. Liu, R. Huang, H. Zhang, X. Li, F. P. García de Arquer, Z. Liu, Y. Li, B. Zhang, *Nat. Commun.* **2022**, *13*, 4871.
[10] R. S. Sherbo, R. S. Delima, V. A. Chiykowski, B. P. MacLeod, C. P. Berlinguette, *Nat. Catal.* **2018**, *1*, 501.
[11] G. Chen, X. Li, X. Feng, *Angew. Chem., Int. Ed.* **2022**, *61*, 202209014.
[12] L. Sha, K. Ye, J. Yin, K. Zhu, K. Cheng, J. Yan, G. Wang, D. Cao, *Chem. Eng. J.* **2020**, *381*, 122603.
[13] B. K. Boggs, R. L. King, G. G. Botte, *Chem. Commun.* **2009**, *32*, 4859.
[14] G. Bharath, F. Banat, *ACS Appl. Mater. Interfaces* **2021**, *13*, 24643.
[15] W. Chen, C. Xie, Y. Wang, Y. Zou, C.-L. Dong, Y.-C. Huang, Z. Xiao, Z. Wei, S. Du, C. Chen, B. Zhou, J. Ma, S. Wang, *Chem* **2020**, *6*, 2974.
[16] J. Hao, J. Liu, D. Wu, M. Chen, Y. Liang, Q. Wang, L. Wang, X.-Z. Fu, J.-L. Luo, *Appl. Catal., B: Enviorn.* **2021**, *281*, 119510.
[17] F. Li, C. Liu, H. Lin, Y. Sun, H. Yu, S. Xue, J. Cao, X. Jia, S. Chen, *J. Colloid Interface Sci.* **2023**, *640*, 329.
[18] Y. Yan, H. Zhou, S.-M. Xu, J. Yang, P. Hao, X. Cai, Y. Ren, M. Xu, X. Kong, M. Shao, Z. Li, H. Duan, *J. Am. Chem. Soc.* **2023**, *145*, 6144.
[19] Y. Xu, M. Liu, S. Wang, K. Ren, M. Wang, Z. Wang, X. Li, L. Wang, H. Wang, *Appl. Catal., B* **2021**, *298*, 120493.
[20] R. Luo, Y. Li, L. Xing, N. Wang, R. Zhong, Z. Qian, C. Du, G. Yin, Y. Wang, L. Du, *Appl. Catal., B: Enviorn.* **2022**, *311*, 121357.
[21] S. Li, S. Wang, Y. Wang, J. He, K. Li, Y. Xu, M. Wang, S. Zhao, X. Li, X. Zhong, J. Wang, *Adv. Funct. Mater.* **2023**, *33*, 2214488.
[22] Y. Li, Y. Jiao, H. Yan, G. Yang, Y. Liu, C. Tian, A. Wu, H. Fu, *Angew. Chem., Int. Ed.* **2023**, *62*, 202306640.
[23] X. Liu, X. He, Z. Fang, S. Gong, D. Xiong, W. Chen, J. Wang, Z. Chen, *Chem. Mater.* **2024**, *36*, 968.
[24] X. Jia, H. Kang, X. Yang, Y. Li, K. Cui, X. Wu, W. Qin, G. Wu, *Appl. Catal., B: Enviorn.* **2022**, *312*, 121389.
[25] R. Peng, Y. Jiang, C.-L. Dong, T. T. Thuy Nga, Y. Lu, S. Li, Y. Fan, C. Xie, S. Wang, Y. Zou, *J. Mater. Chem. A* **2023**, *11*, 15196.
[26] T.-G. Vo, P.-Y. Ho, C.-Y. Chiang, *Appl. Catal., B: Enviorn.* **2022**, *300*, 120723.
[27] J. Chang, F. Song, Y. Hou, D. Wu, F. Xu, K. Jiang, Z. Gao, *J. Colloid Interface Sci.* **2024**, *665*, 152.
[28] H. Chi, J. Lin, S. Kuang, M. Li, H. Liu, Q. Fan, T. Yan, S. Zhang, X. Ma, *J. Energy Chem.* **2023**, *85*, 267.
[29] T. Hui, H. Liu, T. Li, J. Pan, T. Zheng, R. Zhang, X. Meng, H. Liu, Z. Liu, C. Xu, *Appl. Catal. B: Environ. Energy* **2024**, *355*, 124147.
[30] O. A. Rusu, W. F. Hoelderich, H. Wyart, M. Ibert, *Appl. Catal. B: Environ. Energy* **2015**, *176–177*, 139.
[31] A. H. Touny, R. H. Tammam, M. M. Saleh, *Appl. Catal. B: Enviro. Energy* **2017**, *224*, 1017.
[32] Y. Li, C. Wang, L. Yang, W. Ge, J. Shen, Y. Zhu, C. Li, *Adv. Energy Mater.* **2024**, *14*, 2303863.
[33] J. Liu, Y. Li, X. Jia, J. Shen, Y. Zhu, C. Li, *Small* **2025**, *21*, 2408279.
[34] X. Xu, X. Song, X. Liu, H. Wang, Y. Hu, J. Xia, J. Chen, M. Shakouri, Y. Guo, Y. Wang, *ACS Sustainable Chem. Eng.* **2022**, *10*, 5538.
[35] D. Yang, Q. Yu, L. Gao, L. Mao, J.-H. Yang, *Appl. Surf. Sci.* **2017**, *416*, 503.

[36] Y. Qi, Y. Zhang, L. Yang, Y. Zhao, Y. Zhu, H. Jiang, C. Li, *Nat. Commun.* **2022**, *13*, 4602.
[37] J. Chen, E. Quattrocchi, F. Ciucci, Y. Chen, *Chem* **2023**, *9*, 2267.
[38] J. Li, L. Li, X. Ma, X. Han, C. Xing, X. Qi, R. He, J. Arbiol, H. Pan, J. Zhao, J. Deng, Y. Zhang, Y. Yang, A. Cabot, *Adv. Sci.* **2023**, *10*, 2300841.
[39] Y. Li, X. Wei, L. Chen, J. Shi, M. He, *Nat. Commun.* **2019**, *10*, 5335.
[40] X. Liu, R. Wang, M. Wei, X. Wang, J. Qiu, J. Zhang, S. Li, Y. Chen, *J. Colloid Interface Sci.* **2024**, *657*, 438.
[41] B. Zhu, B. Dong, F. Wang, Q. Yang, Y. He, C. Zhang, P. Jin, L. Feng, *Nat. Commun.* **2023**, *14*, 1686.
[42] B. Tian, F. Wang, P. Ran, L. Dai, Y. Lv, Y. Sun, Z. Mu, Y. Sun, L. Tang, W. A. Goddard, M. Ding, *Nat. Commun.* **2024**, *15*, 10145.
[43] S. Rezaee, S. Shahrokhian, *Appl. Catal., B: Enviorn.* **2019**, *244*, 802.
[44] R. Que, M. Li, H. Yao, X. Wang, F. Liao, M. Shao, *ChemSusChem* **2020**, *13*, 964.
[45] B. Zhang, Z. Li, Y. Zhou, Z. Yang, Z. Xue, T. Mu, *Small* **2024**, *20*, 2306663.